

Probing the Solvent Shell with ^{195}Pt Chemical Shifts: Density Functional Theory Molecular Dynamics Study of Pt^{II} and Pt^{IV} Anionic Complexes in Aqueous Solution

Lionel A. Truflandier and Jochen Autschbach*

Department of Chemistry, 312 Natural Sciences Complex, State University of New York, Buffalo, New York 14260-3000

Received November 15, 2009; E-mail: jochena@buffalo.edu

Abstract: Ab initio molecular dynamics (aiMD) simulations based on density functional theory (DFT) were performed on a set of five anionic platinum complexes in aqueous solution. ^{195}Pt nuclear magnetic shielding constants were computed with DFT as averages over the aiMD trajectories, using the two-component relativistic zeroth-order regular approximation (ZORA) in order to treat relativistic effects on the Pt shielding tensors. The chemical shifts obtained from the aiMD averages are in good agreement with experimental data. For $\text{Pt}(\text{II})$ and $\text{Pt}(\text{IV})$ halide complexes we found an intermediate solvent shell interacting with the complexes that causes pronounced solvent effects on the Pt chemical shifts. For these complexes, the magnitude of solvent effects on the Pt shielding constant can be correlated with the surface charge density. For square-planar Pt complexes the aiMD simulations also clearly demonstrate the influence of closely coordinated non-equatorial water molecules on the Pt chemical shift, relating the structure of the solution around the complex to the solvent effects on the metal NMR chemical shift. For the complex $[\text{Pt}(\text{CN})_4]^{2-}$, the solvent effects on the Pt shielding constant are surprisingly small.

1. Introduction

The ^{195}Pt isotope (nuclear spin $I = 1/2$ and natural abundance of about 34%) is a sensitive probe to study platinum chemistry by NMR.^{1–3} Unlike many other transition metal nuclei, ^{195}Pt NMR has been measured routinely for many years, and therefore Pt is among the most frequently studied metal nuclei in NMR.⁴ The presently known chemical shift range of ^{195}Pt is about 13 000 ppm. Platinum chemical shifts are very sensitive not only to ligand substitutions^{4,5} but also to solvent and thermal effects.^{1,6}

The NMR parameters of heavy metal nuclei such as Pt pose particular challenges for quantum mechanics based methodology. On one hand there are the “usual” difficulties associated with first-principles theory such as treating electron correlation and relativistic effects in calculations on metal complexes—which tend to have large electron counts and metal NMR parameters that are sensitive to the various approximations made in the calculations.^{7–10} Routine computations of Pt chemical shifts have therefore not been feasible prior to the development of fast relativistic NMR methods based on density functional theory (DFT). Despite the fact that reasonably fast computer codes for Pt NMR computations are now available,^{10,11} it remains a

challenge to accurately predict Pt chemical shifts in solution or in the solid state due to their sensitivity to the nature of the ligands, to the structure of the complexes, and to the magnitude of solvent effects or electrostatic interactions from a crystal environment.

In particular, the calculation of metal NMR parameters in solution requires elaborate computational models.^{6,9–12} However, this challenge—if it can be overcome—also provides a great opportunity to obtain important new information about how solvation influences the structure of a metal complex and how such structural effects combined with the presence of solvent, in turn, influence the NMR parameters of the metal center. Furthermore, the trends observed for solvent effects on sensitive metal NMR parameters such as ^{195}Pt chemical shifts might perhaps be used by researchers to probe the liquid structure around the solute.

In pioneering first-principles computations of Pt shifts, acceptable agreement with experiment was obtained only when a complex similar to the probe was used as a reference.^{13–17} This indicates that a significant degree of error cancellation was

- (1) Pregosin, P. S. *Coord. Chem. Rev.* **1982**, *44*, 247–291.
- (2) Pregosin, P. *Annu. Rep. NMR Spectrosc.* **1986**, *17*, 285–349.
- (3) Pregosin, P. S. *Transition Metal Nuclear Magnetic Resonance*; Elsevier Publishing Co.: Amsterdam, 1991.
- (4) Priqueler, J. R. L.; Butler, I. S.; Rochon, F. D. *Appl. Spectrosc. Rev.* **2006**, *41*, 185.
- (5) Still, B. M.; Kumar, P. G. A.; Aldrich-Wright, J. R.; Price, W. S. *Chem. Soc. Rev.* **2007**, *36*, 665–686.
- (6) Sterzel, M.; Autschbach, J. *Inorg. Chem.* **2006**, *45*, 3316–3324.
- (7) Facelli, J. C. *Concepts Magn. Reson.* **2004**, *20A*, 42–69.

- (8) Kaupp, M.; Bühl, M.; Malkin, V. G. *Calculation of NMR and EPR Parameters: Theory and Applications*; Wiley-VCH: Weinheim, 2004.
- (9) Bühl, M. *Annu. Rep. NMR Spectrosc.* **2008**, *64*, 77–126.
- (10) Autschbach, J.; Zheng, S. *Annu. Rep. NMR Spectrosc.* **2009**, *67*, 1–95.
- (11) Autschbach, J. Calculation of heavy-nucleus chemical shifts: Relativistic all-electron methods. In *Calculation of NMR and EPR Parameters. Theory and Applications*; Kaupp, M., Bühl, M., Malkin, V. G., Eds.; Wiley-VCH: Weinheim, 2004.
- (12) Bühl, M. NMR of transition metal compounds In *Calculation of NMR and EPR Parameters. Theory and Applications*; Kaupp, M., Bühl, M., Malkin, V. G., Eds.; Wiley-VCH: Weinheim, 2004; pp 421–431.
- (13) Gilbert, T. M.; Ziegler, T. *J. Phys. Chem. A* **1999**, *103*, 7535–7543.
- (14) Autschbach, J.; Guennic, B. L. *Chem.—Eur. J.* **2004**, *10*, 2581–2589.

underlying the good agreement with experiment. A recent study of somewhat preliminary character has provided strong indications that accurate computations of Pt chemical shifts require a computational model that includes solvent effects at a level of detail such that solvent–solute interactions affect differently coordinated complexes in different ways (i.e., square-planar Pt^{II} versus octahedral Pt^{IV}).⁶ Moreover, it was found that the Pt chemical shift, in particular in negatively charged complexes, is very sensitive to the metal–ligand bond distances, which are in turn, to some extent, influenced by explicit solvent effects. A structural sensitivity of NMR in negatively charged complexes was also previously noted by Bühl et al.^{18–20} The previous paper from our group⁶ concluded that good agreement of computed Pt chemical shifts with experiment is likely to require a fully dynamic model where solvent effects on the complexes' structure as well as the solvent structure around the complexes is modeled at a high level of theory. It is our aim to demonstrate here that this is indeed the case and that much can be learned about solvation of metal complexes from its effects on metal chemical shifts.

For the present study we have therefore decided to compute the Pt NMR chemical shifts of a set of negatively charged Pt complex ions {[PtCl₄]^{2−}, [PtCl₆]^{2−}, [PtBr₄]^{2−}, [PtBr₆]^{2−}, [Pt(CN)₄]^{2−}} based on ab initio molecular dynamics (aiMD) with solvent (H₂O) treated explicitly by quantum mechanics. We have obtained several rather surprising results that are reported in this work. For example, while solvent effects on the Pt shielding constants of the halide complexes are significant, the Pt shielding in [Pt(CN)₄]^{2−} remains virtually unchanged between gas phase and solution. Further, the halide complexes afford an intermediate solvation shell that behaves markedly differently from the solvent bulk, while such an intermediate shell is not seen for [Pt(CN)₄]^{2−}. The intermediate shell is found both for the octahedral Pt^{IV} and for the square-planar Pt^{II} halide complexes. Overall, the calculated chemical shifts after time averaging are within about 5% of the experimental shifts, which is very satisfactory considering that different Pt oxidation states, complex geometries with and without open coordination sites, and different types of ligands are involved. A direct correlation between the solution structure of heavy metal complexes and their respective metal NMR shielding constants—or chemical shifts—is demonstrated. Analysis of the aiMD radial distribution functions shows that the number of solvent molecules present in the first—or intermediate—solvation shell is related to the number of nearest solvent molecules needed to reach converge of the time-averaged chemical shifts. First attempts at rationalization suggest that the strength of the solvent-induced ¹⁹⁵Pt magnetic shieldings is correlated to the charge density per surface unit of the anionic complexes. An analysis of the influence of vibrational effects on the Pt chemical shifts was also performed. Despite the very strong dependence of the Pt shielding on the Pt–ligand bond distances, the aiMD averages without solvent yielded only <100 ppm changes with respect

to a static calculation, indicating that direct electronic solvent effects and the solvent-induced changes of the average geometries are predominant.

To our knowledge this is the first time that NMR chemical shifts for a “relativistic nucleus” like Pt have been computed on the basis of aiMD followed by relativistic NMR chemical shift density functional calculations. Therefore, we hope that this study will also contribute some much needed development of computational protocols to this area of research. For aiMD-based studies of chemical shifts of 3d and 4d metals, we refer the reader to the excellent work by Bühl and co-workers.^{18–22}

This paper is organized as follows: In section 2, details of the computational procedure are provided. In section 3, the liquid structures of the solvated Pt complexes are presented and critically assessed with respect to the available experimental and theoretical data. The reliability of the time-dependent simulation is discussed in terms of vibrational density of states in section 4, leading into the computation of the time-average ¹⁹⁵Pt isotropic shielding constants presented in section 5. Analyses of the vibrational-, solvent-, structural- and relativity-induced effects on the Pt shielding constants and chemical shifts are discussed in sections 6 and 7. A few concluding remarks and an outlook can be found in section 8.

2. Computational Details

Ab initio molecular dynamics (aiMD) studies have been carried out within the Car–Parrinello (CP) framework,²³ using the Quantum-ESPRESSO suite of programs.²⁴ The generalized gradient approximation (GGA) of the exchange–correlation potential proposed by Perdew, Burke, and Ernzerhof (PBE) has been used,²⁵ in conjunction with ultrasoft pseudopotentials (USPPs)²⁶ and a plane wave (PW) basis set to expand the valence orbitals. The core levels and radii (given in atomic units, au) were [He](1.5,1.3,1.2), [Ne](1.5), [Ar + 3d](1.8), [Xe + 4f](1.8) for (C,N,O), Cl, Br, and Pt, respectively. For hydrogen, an “all-electron pseudopotential” was generated with a core radius of 0.9 au.

The reliability of these atomic potentials was checked against molecular quantum chemical calculations with pseudopotentials by realizing a set of test calculations based on geometry optimization. For the latter, a quantum molecular code was employed,²⁷ in combination with the all-electron Gaussian-type orbital (GTO) basis set of Hay et al. for all the elements,²⁸ except Pt, Cl, and Br, where effective core potentials (ECPs) were used.^{29,30} The USPPs of the Pt, Cl, and Br atoms were constructed using the Koelling–Harmon relativistic formulation of the radial Schrödinger equation,³¹ together with the PBE functional. A set of neutral {PtCl₂(CO)₂, PtCl₂(NH₃)₂, Pt₂Cl₄(CO)₂} and charged {[PtCl₄]^{2−}, [PtCl₆]^{2−}, [PtBr₄]^{2−}, [PtBr₆]^{2−}, [Pt(CN)₄]^{2−}, [Pt(CN)₆]^{2−}} Pt complexes was optimized, setting the residual force tolerance to 10^{−4} au for both the PW and the GTO approaches. In the former case, a cubic box of dimension 13 Å was used. Analysis of the main geometrical parameters has shown a mean deviation of <2% for the Pt–X distances and 1% for the

(15) Guennic, B. L.; Matsumoto, K.; Autschbach, J. *Magn. Reson. Chem.* **2004**, *42*, S99–S116.

(16) Fowe, E. P.; Belser, P.; Daul, C.; Chermette, H. *Phys. Chem. Chem. Phys.* **2005**, *7*, 1732–1738.

(17) Koch, K. R.; Burger, M. R.; Kramer, J.; Westra, A. N. *Dalton Trans.* **2006**, 3277–3284.

(18) Bühl, M.; Mauschick, F. T. *Phys. Chem. Chem. Phys.* **2002**, *4*, 5508–5514.

(19) Bühl, M.; Mauschick, F. T.; Mauschick, F. T.; Terstegen, F.; Wrackmeyer, B. *Angew. Chem., Int. Ed.* **2002**, *41*, 2312–2315.

(20) Bühl, M.; Grigoleit, S.; Kabrede, H.; Mauschick, F. T. *Chem.—Eur. J.* **2006**, *12*, 477–488.

(21) Bühl, M.; Parrinello, M. *Chem.—Eur. J.* **2001**, *7*, 4487–4494.

(22) Bühl, M. *J. Phys. Chem. A* **2002**, *106*, 10505–10509.

(23) Car, R.; Parrinello, M. *Phys. Rev. Lett.* **1985**, *55*, 2471.

(24) Giannozzi, P.; et al. *J. Phys.: Condens. Matter* **2009**, *21*, 395502.

(25) Perdew, J. P.; Burke, K.; Ernzerhof, M. *Phys. Rev. Lett.* **1996**, *77*, 3865.

(26) Vanderbilt, D. *Phys. Rev. B* **1990**, *41*, 7892.

(27) Frisch, M. J.; et al. *Gaussian 03*, Revision C.02; Gaussian, Inc.: Wallingford, CT, 2004.

(28) Dunning, J. J. *Chem. Phys.* **1989**, *90*, 1007–1023.

(29) Hay, P. J.; Wadt, W. R. *J. Chem. Phys.* **1985**, *82*, 270–283.

(30) Peterson, K. A.; Figgen, D.; Goll, E.; Stoll, H.; Dolg, M. *J. Chem. Phys.* **2003**, *119*, 11113–11123.

(31) Koelling, D. D.; Harmon, B. N. *J. Phys. C: Solid State Phys.* **1977**, *10*, 3107–3114.

X–Pt–X angles which were not restrained by the symmetry conditions (neutral complexes). Considering the numerous uncertainties which might be a source of discrepancy (such as the residual interactions between the periodic images of the molecules, accuracy of the GTO basis sets, methods used for deriving the ECPs and the USPPs) between the PW and GTO approaches, the agreement obtained here validates the use of the USPPs to represent the heavy atoms' cores. Moreover, during these benchmarks, we found that a kinetic energy and density cutoff of 35 and 320 Ry, respectively, were sufficient to achieve force convergence.

The solvated anionic Pt complexes have been modeled by using a cubic box with 64 water molecules and two protons. The latter have been introduced in order to recover a neutral charge overall. Since the periodic boundary conditions enforce separation of the complex ions, the model approximates an infinitely dilute solution. Residual interactions might still be present between charged species in neighboring unit cells, but we estimate these to be small due to the relatively large simulation cells used. For each Pt complex, the box size has been adapted to reach a mean density of $1.05 \text{ g} \cdot \text{cm}^{-3}$. This leads to box dimensions between 13.3 (obtained for $[\text{PtCl}_4]^{2-} + 64\text{H}_2\text{O} + 2\text{H}^+$) and 14.2 Å (obtained for $[\text{PtBr}_6]^{2-} + 64\text{H}_2\text{O} + 2\text{H}^+$). For the structural studies discussed below, the same constraints were applied to build a "pure" 64 H_2O box. CP molecular dynamics were performed by using a fictitious electron mass of 450 au and a time step of 5 au (0.0121 fs). Ions and electrons were both propagated using the velocity-Verlet algorithm.³² Simulations were performed over 2 ps in the NVT ensemble prior to 5 ps of production run within the microcanonical (NVE) ensemble. In the former case, a Nosé–Hoover thermostat chain was applied to keep the temperature at 300 K.^{33,34} A sampling period of 0.24 fs (every 20 steps) was used to evaluate the radial distributions functions (RDFs) and the velocity autocorrelation functions (VACFs). The methodology used for the calculations of these dynamical properties and the power density spectrum related to the vibrational density of states are presented in the Supporting Information (SI).

DFT calculations of the ^{195}Pt NMR shielding tensor have been performed using the Amsterdam density functional (ADF) program suite.³⁵ Incorporation of relativistic effects into the NMR calculations has been realized by the zeroth-order regular approximation (ZORA) of the Dirac equation,³⁶ using the approach developed by Wolff et al.³⁷ As previously argued, combination of the revised PBE functional³⁸ with ZORA-optimized triple- ζ singly polarized (TZP) and quadruple- ζ quadruply polarized (QZ4P) Slater-type orbital (STO) basis sets for the ligand atoms and Pt,³⁹ respectively, leads to reliable results for the calculation of ^{195}Pt chemical shifts.⁶ In this work, the triple- ζ singly polarized basis has been replaced by its doubly polarized analogue (TZ2P) in order to yield a better description of the weak hydrogen-bonding-type interactions occurring between Pt ligands and water molecules. For the latter, the TZ2P basis sets provided by the ADF basis set library have been employed. In section 3 a comparison of the mean structural parameters deduced from the CP-aiMDs with geometries obtained from ZORA-STO optimized stationary points will be presented. In the latter case, a combination of the scalar-relativistic ZORA Hamiltonian and QZ4P basis set for all the atoms was employed, along with the conductor-like screening model (COSMO) to

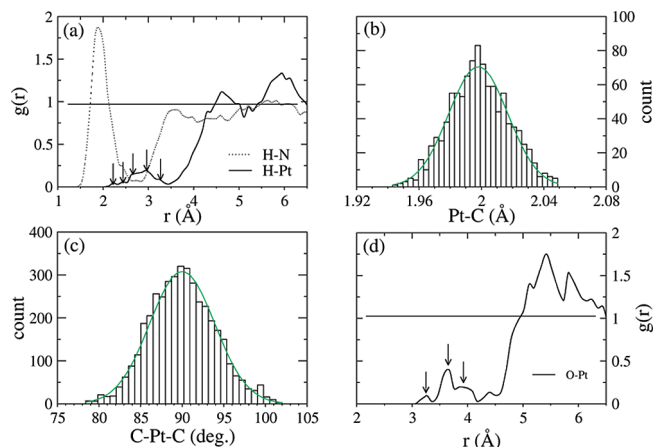


Figure 1. (a) Partial radial distribution functions for N–H and Pt–H atom pairs for the solvated complex $[\text{Pt}(\text{CN})_4]^{2-}$. (b,c) Pt–C distance and C–Pt–C angle distributions. Gaussian distributions using the parameters of Table 2 are also plotted (green line) and serve as a guide to the eye. (d) Partial radial distribution function for the Pt–O atom pair. The arrows point out the presence of direct Pt– H_2O and/or Pt– OH_2 interactions along the axis perpendicular to the square-planar Pt complexes (see Figure 3).

simulate the solvent effects.^{40–42} The atomic radii given in ref 14 were used to construct the solvent cavity. We report chemical shifts with respect to the standard reference $[\text{PtCl}_6]^{2-}$. Calculated absolute shielding constants are provided here and in the SI to facilitate conversion to another reference among the set of complexes studied here (see eq 4).

3. Structural Analysis

Characterizations of the bulk liquid structure for the various solvated Pt complexes have been realized through the analysis of the RDFs. As an example, the water structure related to the solvated $[\text{PtCl}_4]^{2-}$ system (noted $[\text{PtCl}_4]_{\text{sol}}^{2-}$) is described in the SI, along with pure water simulations for comparison. It should be noticed here that the latter is in good agreement with recent X-ray scattering experiments^{43,44} and previous theoretical studies,^{45,46} focusing on the water structure at room temperature. We shall focus here on RDFs involving solute atoms.

The analysis of the X–H RDFs, relating the distance distribution between X (X = Cl, Br, N) and the solvent protons, allows us to evaluate the mean distance and the number of water molecules directly bound to the Pt complexes through the ligand. Radial distributions are plotted in Figure 1a and Figure S2 (SI) for $[\text{Pt}(\text{CN})_4]_{\text{sol}}^{2-}$ and $[\text{PtX}_n]_{\text{sol}}^{2-}$, respectively. The principal structural parameters obtained from these data are collected in Table 1. We observe that the H–X distances increase along the set $\text{CN} > \text{Cl} > \text{Br}$, with the peaks around 1.9, 2.3, and 2.5 Å for $[\text{Pt}(\text{CN})_4]_{\text{sol}}^{2-}$, $[\text{PtCl}_n]_{\text{sol}}^{2-}$, and $[\text{PtBr}_n]_{\text{sol}}^{2-}$, respectively. While the mean X–H distance depends upon the ligand atom attached to the metal, the average number of water molecules in close proximity to the complex is related to its geometry, i.e., square-

(32) Verlet, L. *Phys. Rev.* **1967**, *159*, 98.

(33) Nose, S. *J. Chem. Phys.* **1984**, *81*, 511–519.

(34) Hoover, W. G. *Phys. Rev. A* **1985**, *31*, 1695.

(35) Baerends, E. J.; et al. *ADF 2006.01, SCM*; Theoretical Chemistry, Vrije Universiteit: Amsterdam, 2006.

(36) van Lenthe, E.; Baerends, E. J.; Snijders, J. G. *J. Chem. Phys.* **1993**, *99*, 4597–4610.

(37) Wolff, S. K.; Ziegler, T.; van Lenthe, E.; Baerends, E. J. *J. Chem. Phys.* **1999**, *110*, 7689–7698.

(38) Hammer, B.; Hansen, L. B.; Nørskov, J. K. *Phys. Rev. B* **1999**, *59*, 7413.

(39) Lenthe, E. V.; Baerends, E. J. *J. Comput. Chem.* **2003**, *24*, 1142–1156.

(40) Klamt, A.; Schuurmann, G. *J. Chem. Soc., Perkin Trans. 2* **1993**, 799–805.

(41) Klamt, A. *J. Phys. Chem.* **1996**, *100*, 3349–3353.

(42) Pye, C. C.; Ziegler, T. *Theor. Chem. Acc.* **1999**, *101*, 396–408.

(43) Soper, A. K.; Bruni, F.; Ricci, M. A. *J. Chem. Phys.* **1997**, *106*, 247–254.

(44) Sorenson, J. M.; Hura, G.; Glaeser, R. M.; Head-Gordon, T. *J. Chem. Phys.* **2000**, *113*, 9149–9161.

(45) Grossman, J. C.; Schwegler, E.; Draeger, E. W.; Gygi, F.; Galli, G. *J. Chem. Phys.* **2004**, *120*, 300–311.

(46) Schwegler, E.; Grossman, J. C.; Gygi, F.; Galli, G. *J. Chem. Phys.* **2004**, *121*, 5400–5409.

Table 1. Description of the X–H Interactions According to the Radii of the Innermost $g_{\text{XH}}(r)$ RDFs Maxima, along with the Integration Radii (r_{int}) Used To Calculate the Number of Coordination (n_{XH})^a

	complex				
	[PtCl ₄] _{sol} ^{2−}	[PtBr ₄] _{sol} ^{2−}	[Pt(CN) ₄] _{sol} ^{2−}	[PtCl ₆] _{sol} ^{2−}	[PtBr ₆] _{sol} ^{2−}
$g_{\text{XH}}(r)$	X = Cl	X = Br	X = N	X = Cl	X = Br
r_{max} (Å) ^b	2.29	2.48	1.89	2.28	2.50
r_{int} (Å)	2.9	3.0	2.8	2.8	3.1
n_{XH}	2.5	2.1	2.5	1.4	1.6
$g_{\text{PtO}}(r)$					
r_{max} (Å) ^c	4.79/4.49	5.61/5.38/5.08	5.42/5.83	4.95/4.64	5.02
r_{int} (Å)	5.3	5.8		5.4 (6.0)	5.5 (5.9)
n_{PtO}	12.0	14.0		10.2 (13.8) ^d	9.9 (12.8) ^e

^a The same approach was used to determine the numbers of oxygen atoms in the first water solvation shell (see Figure 2) around the Pt complexes using the $g_{\text{PtO}}(r)$ RDFs. ^b See Figures S2 (SI) and 1a for [PtX₄]_{sol}^{2−} and [Pt(CN)₄]_{sol}^{2−}, respectively. ^c See Figures 2 and 1d for [PtX_n]_{sol}^{2−} and [Pt(CN)₄]_{sol}^{2−}, respectively. ^d The number in parentheses is obtained if we integrate also the sharp peak at 5.74 Å. ^e The number in parentheses is obtained if we integrate also the sharp peak at 5.66 Å.

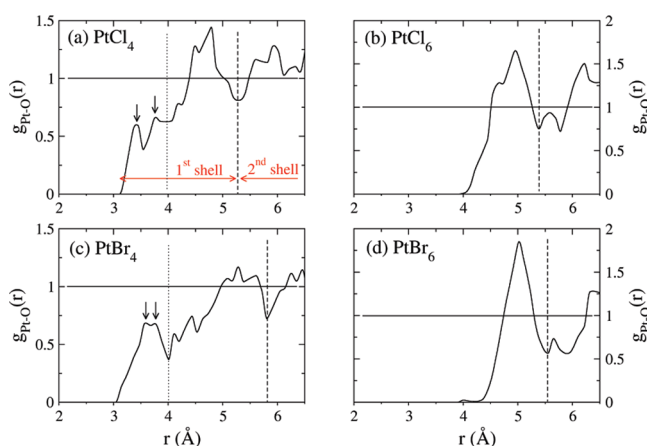


Figure 2. Partial radial distribution functions for Pt–O atom pairs for the solvated [PtX_n]_{sol}^{2−} complexes. The vertical dashed line represents the separation between the first and second solvation shells. For the former, the number of water molecules is given in Table 1. Arrows describe the presence of direct Pt–H₂O and/or Pt–OH₂ interactions along the axis perpendicular to the square-planar Pt complexes. The vertical dotted lines indicate the integration radius used for calculation of the O coordination number given in Table 2.

planar vs octahedral. The hydrogen coordination numbers obtained for the various complexes (Table 1) show that each ligand atom of the [PtX₄]_{sol}^{2−} complexes is involved in more than two H-bonds, independent of the ligand type X, compared to an average of 1.5 H-bonds for the octahedral [PtX₆]_{sol}^{2−}.

Pt–O RDFs for the chlorine and bromine complexes are shown in Figure 2, and the related principal structural parameters are collected in Table 1. The similarities between the forms of the Pt–O RDFs obtained for [PtCl₄]_{sol}^{2−} and [PtBr₄]_{sol}^{2−} on one hand, and [PtCl₆]_{sol}^{2−} and [PtBr₆]_{sol}^{2−} on the other hand, demonstrate that the structure of the hydration shell is dependent on the complex geometry but to a lesser extent on the type of halide. It should be noticed, however, that the Pt–O RDF of the [Pt(CN)₄]_{sol}^{2−} complex (Figure 1d) completely differs from those of the halide complexes, indicating a strong influence of the ligand type on the hydration shell structure. This result is reinforced by comparing the overall shape of the X–H RDFs obtained for the [PtX_n]_{sol}^{2−} set of complexes with the cyanide analogue, for which we observe a well-defined signature of the N–H hydrogen bonds at 1.89 Å. Despite the presence of several peak shoulders and secondary maxima on the Pt–O RDFs (Table 1), an intermediate solvation shell appears between 3.0 and 5.5 Å for the [PtX_n]_{sol}^{2−} complexes, whereas this characteristic seems to be absent for [Pt(CN)₄]_{sol}^{2−}.

Further evidence for profound differences between the solutions of halide and cyano complexes is provided by the analysis of the variation of the Pt–O RDFs: Within the range of 5.0–6.0 Å, the $g_{\text{PtO}}(r)$ minimum (around 0.75) for the halide complexes is found to be below the reference value of 1, indicating a partial de-correlation between the first (or intermediate) and the second hydration shells (Figure 2a). Conversely, the fact that this feature is absent in the $g_{\text{PtO}}(r)$ of [Pt(CN)₄]_{sol}^{2−} suggests that there is no formation of an intermediate shell for the cyanide Pt complex within the range of 3.0–6.5 Å. The size of the model, i.e., the length *L* of the simulation box, used for these calculations limits further conclusions. Following the periodic minimum image convention,⁴⁷ the calculated *g*(*r*) has a physical meaning only for *r* ≤ *L*/2. As a result, with the box size employed in this study, a reliable description of the hydration shell is possible only within a sphere of radius 6.5 Å centered around the Pt nucleus. These limitations do not affect the conclusions drawn for the solvated [PtX_n]_{sol}^{2−} complexes, for which the splitting between the two solvent shells is around 5.5 Å, whereas size effects might be present for [Pt(CN)₄]_{sol}^{2−} if the first hydration shell extends over 6.5 Å. On the basis of the calculation of the ¹⁹⁵Pt chemical shift as a function of the water shell size, in section 6 we will provide further support that the formation of an intermediate solvent structure seems to occur only for halide complexes.

The theoretical number of water molecules arising from the Pt–O RDF integrations and defining the first solvation shell is between 10 and 14 for the [PtX_n]_{sol}^{2−} complexes (see Table 1). The number of water molecules is somewhat higher for square-planar complexes, with 12 and 14 for [PtCl₄]_{sol}^{2−} and [PtBr₄]_{sol}^{2−}, respectively, compared to 10 or higher for the [PtX₆]_{sol}^{2−} complexes. The numbers of water molecules become more consistent if, for the hexahalides, a sharp maximum following the main first solvent peak in g_{PtO} is included in the integration. Since the radial distribution functions give access to only an isotropic fingerprint of the solvent shell structure, which in our case could be strongly anisotropic, some uncertainties concerning the counting of the number of water molecules remain. Extension of radial distribution analysis to angular-resolved functions based on spherical harmonics decompositions⁴⁷ should improve the accuracy of our analysis and will be the subject of future studies. Besides these limitations, the number of water molecules constituting the intermediate solvation shell predicted in this work is consistent with previous works focusing on the modeling of platinum chloro complexes in aqueous solution

(47) Frenkel, D.; Smit, B. *Understanding Molecular Simulation: From Algorithms to Applications*, 2nd ed.; Academic Press: New York, 2001.

Table 2. Pt–H₂O and Pt–OH₂ Axial Interactions in the Square-Planar Complexes (See Figure 3) Obtained from the Radii of the $g_{\text{PtH}}(r)$ and $g_{\text{PtO}}(r)$ Maxima (r_{max}) along with the Radii Used for the RDF Integrations (r_{int}), Allowing the Calculation of the Coordination Numbers n_{PtH} and n_{PtO} , Respectively

	complex		
	[PtCl ₄] _{sol} ^{2−}	[PtBr ₄] _{sol} ^{2−}	[Pt(CN) ₄] _{sol} ^{2−}
$g_{\text{PtH}}(r)$			
r_{max} (Å) ^a	2.42/2.84	2.41/2.80	2.23/2.44/2.64 2.94/3.24
r_{int} (Å)	3.2	3.2	3.4
n_{PtH}	2.0	1.7	0.7
$g_{\text{PtO}}(r)$			
r_{max} (Å) ^b	3.42/3.77	3.58/3.76	3.26/3.64 3.86
r_{int} (Å)	4.0	4.0	4.2
n_{PtO}	2.3	1.8	0.8

^a See Figure S3 in the SI and Figure 1a for [PtX₄]_{sol}^{2−} and [Pt(CN)₄]_{sol}^{2−}, respectively. ^b See Figures 2 and 1d for [PtX₄]_{sol}^{2−} and [Pt(CN)₄]_{sol}^{2−}, respectively.

using classical molecular dynamic.^{48,49} For both [PtCl₄]_{sol}^{2−} and [PtCl₆]_{sol}^{2−}, the first sphere of hydration was found to be around 8 or 10 water molecules, depending of the RDFs used for the integration, i.e., $g_{\text{PtO}}(r)$ or $g_{\text{ClO}}(r)$.

Another interesting structural feature is the presence of weakly bound water molecules along the axial region of [PtX₄]_{sol}^{2−}. Analysis of the [PtCl₄]_{sol}^{2−} and [PtBr₄]_{sol}^{2−} Pt–O RDFs within the range of 3.0–4.0 Å (Figure 2) reveals direct interactions between water and the metal center, whereas for the octahedral analogues, these characteristics are absent. The Pt–H RDFs confirm these results by displaying two weakly resolved peaks around 2.4 and 2.8 Å for both the chlorine and bromine square-planar complexes (see Figure S3 in the SI and Table 2). It should be noted that, for [Pt(CN)₄]_{sol}^{2−}, the same feature is observed (Figure 1a) but with a lower probability (for example, $g_{\text{PtH}}(3.0) \approx 0.5$ and 0.2 for the Pt–H RDFs of [PtCl₄]_{sol}^{2−} and [Pt(CN)₄]_{sol}^{2−}, respectively). The $g_{\text{PtH}}(r)$ and $g_{\text{PtO}}(r)$ integrate to 2.0, 1.7, and 0.7 hydrogen and 2.3, 1.8, and 0.8 oxygen atoms for [PtCl₄]_{sol}^{2−}, [PtBr₄]_{sol}^{2−}, and [Pt(CN)₄]_{sol}^{2−}, respectively (Table 2). This indicates that, on average, the halide complex axial region is occupied by two water molecules (probably above and below the square plane), whereas less than one is observed for [Pt(CN)₄]_{sol}^{2−}. These results are consistent with previous studies describing the hydration structure of square-planar aqua ions such as [Pt(H₂O)₄]²⁺ and [Pd(H₂O)₄]²⁺.^{50–53} The authors have shown that the two modes of interaction depicted in Figure 3, i.e., the anionic (Pt–H₂O) and ion–dipole (Pt–OH₂) orientations, are involved in the presence of water molecules in the nonequatorial regions of the Pt^{II} and Pd^{II} aqua ions.^{50–52} Moreover, it was demonstrated that the presence of such axial water molecules is mainly induced by the surrounding bulk water and that this effect cannot be properly recovered by using a static quantum molecular approach.⁵²

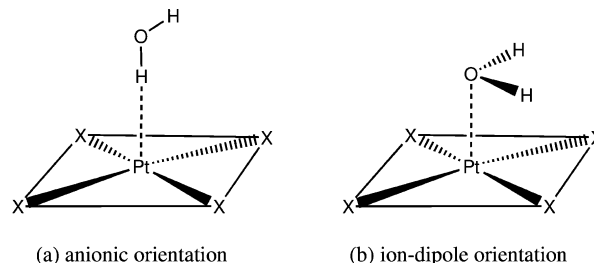


Figure 3. Schemes of the two main modes of interaction between a water molecule and the Pt center in the solvated [PtX₄]_{sol}^{2−} (X = Cl, Br, CN) square-planar complexes. The symbolic notations Pt–H₂O and Pt–OH₂ are used in the text to define the interaction type (a) and (b), respectively.

As remarked by Martínez et al.,⁵⁰ the axial hydration region should be viewed as a time-dependent property: The water exchange occurring close to the metal center is characterized by a mean residence time which is much lower than the bulk motion (4 vs 12 ps, respectively). This might also explain the difficulties associated with experimental detection of axial water molecules for the solvated [PtCl₄]_{sol}^{2−} and [Pt(H₂O)₄]²⁺ ions,⁵⁴ which contrasts with the recent combined theoretical/experimental results published for the hydrated Pt^{II} in aqueous solution.⁵⁵ We emphasize that previous classical MD simulations of the [PtCl₄]_{sol}^{2−} and [PtCl₆]_{sol}^{2−} complexes in aqueous solution have found no evidence of the presence of axial Pt–H₂O and Pt–OH₂ interactions,⁴⁹ which might be due to the limitation of the model potential used for the computations. This is supported by the fact that another work dealing with the classical MD simulation of the Pd^{II} in aqueous solution, using a more elaborate interaction potential, has revealed the presence of weakly bound water molecules in the axial region of the square-planar complex.⁵⁰

Mean Pt–X distances and mean X–Pt–X angles from the CP-aiMDs are collected in Table 3, along with the their respective standard deviations. The latter show that, on average, the square-planed and octahedral geometries of [PtX₄]_{sol}^{2−} and [PtX₆]_{sol}^{2−} are conserved. The Gaussian-like distributions of the Pt–X distances and X–Pt–X angles centered around 2.35 Å and 90.0° for [Pt(CN)₄]_{sol}^{2−} (Figure 1b and c, respectively) which are also observed for the halides complexes, support this result. Comparison of the computed mean Pt–X distances with liquid-state extended X-ray absorption fine structure (EXAFS, available only for [PtCl₄]_{sol}^{2−} and [PtCl₆]_{sol}^{2−}) and X-ray diffraction (XRD) data gathered in Table 3, is consistent with the well-known trend of the GGA functionals to overestimate bond lengths somewhat. It should be noted that the observed discrepancies of around 2% between the calculated and experimental bond lengths are also due to a more fundamental uncertainty: There is no evidence that the bulk corrections due to the solvent in liquid-state simulations are identical to the packing effects observed in the solid-state phases. Indeed, it seems that inclusion of solvent corrections using the COSMO approach in order to reproduce condensed-phase effects tends to reduce the Pt–X bond lengths and the discrepancies with solid-state XRD data.⁶¹ From comparison of the mean Pt–X distances obtained from the CP-aiMDs with the optimized geometries including the solvent shell effects through the COSMO approach (Table 3), we obtain a rather remarkable agreement, with deviations lower

(48) Lienke, A.; Klatt, G.; Robinson, D. J.; Koch, K. R.; Naidoo, K. J. *Inorg. Chem.* **2001**, *40*, 2352–2357.

(49) Naidoo, K. J.; Klatt, G.; Koch, K. R.; Robinson, D. J. *Inorg. Chem.* **2002**, *41*, 1845–1849.

(50) Martínez, J. M.; Torricio, F.; Pappalardo, R. R.; Marcos, E. S. *J. Phys. Chem. B* **2004**, *108*, 15851–15855.

(51) Beret, E. C.; Pappalardo, R. R.; Doltsinis, N. L.; Marx, D.; Marcos, E. S. *ChemPhysChem* **2008**, *9*, 237–240.

(52) Beret, E. C.; Martínez, J. M.; Pappalardo, R. R.; Marcos, E. S.; Doltsinis, N. L.; Marx, D. *J. Chem. Theory Comput.* **2008**, *4*, 2108–2121.

(53) Torricio, F.; Pappalardo, R.; Marcos, E.; Martínez, J. *Theor. Chem. Acc.* **2006**, *115*, 196–203.

(54) Ayala, R.; Marcos, E. S.; Diaz-Moreno, S.; Sole, V. A.; Munoz-Paez, A. *J. Phys. Chem. B* **2001**, *105*, 7588–7593.

(55) Hofer, T. S.; Randolf, B. R.; Rode, B. M.; Persson, I. *Dalton Trans.* **2009**, 1512–1515.

Table 3. Principal Structural Parameters of the [PtX_n]^{2−} (X = Cl, Br and n = 4, 6) and [Pt(CN)₄]^{2−} Complexes

complex		Pt–X (Å)	X–Pt–X (deg)
[PtCl ₄] ^{2−}	CP-aiMD ^a	2.346 ± 0.026	90.0 ± 3.9
	ADF-COSMO ^b	2.348	
	EXAFS ^{c,54}	2.304	
	diffraction ^d	2.315	
[PtBr ₄] ^{2−}	CP-aiMD	2.496 ± 0.024	90.1 ± 4.0
	ADF-COSMO	2.491	
	diffraction ⁵⁶	2.445	
[PtCl ₆] ^{2−}	CP-aiMD	2.385 ± 0.021	90.0 ± 4.3
	ADF-COSMO	2.375	
	EXAFS ⁵⁷	2.330	
	diffraction ⁵⁸	2.316	
[PtBr ₆] ^{2−}	CP-aiMD	2.538 ± 0.015	90.0 ± 3.6
	ADF-COSMO	2.532	
	diffraction ⁵⁹	2.463	

complex		Pt–C (Å)	C–N (Å)	C–Pt–C (deg)
[Pt(CN) ₄] ^{2−}	CP-aiMD	1.998 ± 0.019	1.178 ± 0.008	90.0 ± 3.9
	ADF-COSMO	1.999	1.175	
	diffraction ⁶⁰	1.980	1.150	

^a Mean angle and distance values along with the respective standard deviations from the CP-aiMD. ^b From DFT-optimized geometry using the COSMO solvation model (see section 2). ^c From extended X-ray absorption fine structure (EXAFS) realized on aqueous solutions. ^d From neutron or X-ray diffraction measurements.

than 0.4%. These results demonstrate the reliability of the COSMO approach to yield an average geometry of solvated Pt complexes from static geometry optimizations performed on the isolated systems. In hindsight this result to some extent justifies the static computational model for Pt NMR calculation developed in ref 6, but it also highlights the difficulty of judging the reliability of a model on the basis of a single geometry. Namely, the COSMO computations do not offer any insight into the Pt complex hydration shells and the intriguing differences observed between the halides and the cyano complexes.

4. Vibrational Considerations

A complete investigation of all dynamical properties of the solvated [PtX_n]^{2−} complexes is beyond the scope of this paper, but some fundamental vibrational quantities must be calculated and compared to the available experimental data in order to assess the quality of the aiMD trajectories. Indeed, knowing the very high sensitivity of the ¹⁹⁵Pt NMR response to the nature of the ligand,^{4,5} the local geometry of the metallic center, and the solvent shell (especially for anionic complexes),^{6,14} we must achieve a reliable sampling of the configuration space to compute accurate values, within the ZORA-DFT approximations, of the metal chemical shifts. As discussed in the previous section, the mean structures of the solvated Pt complexes computed from the CP-aiMD are in good agreement with the experimental data and optimized geometries obtained from elaborate quantum chemical methods. Bearing in mind known

typical GGA bond length overestimation, one might expect that the GGA approximation affects the dynamical properties by somewhat underestimating the vibrational frequencies.⁶⁴ In this section we discuss the relevance of the aiMD in terms of “dynamical information”, in other words: Is the time of propagation long enough to transfer the essentials of the vibrational signature (both the solvent and the complex) into the computation of the NMR properties?

Atomic velocity autocorrelation functions (VACFs) obtained for [PtCl₄]_{sol}^{2−} and the details of the procedure for these calculations are presented in the SI. The vibrational density of states (VDOS) computed from the power spectrum of the VACFs obtained for the [PtCl₄]_{sol}^{2−} system and pure water are presented in Figure S1d. Comparison of the normalized atomic VACFs in Figure S4a,b demonstrates that, whereas a propagation time of 5 ps is sufficient to obtain complete dynamical information for the solvent, it seems to be borderline for the Pt complex in the simulation cell. As expected, the fast motional regime of water molecules contrasts strongly with the slow vibrational properties of heavy atoms such as Pt and Cl.

The VDOSs computed for the [PtCl₄]_{sol}^{2−} system and pure water are almost identical (Figure S1d). This indicates the predominance of the solvent vibrations with respect to the complex. We emphasize that the calculated VDOSs are consistent with Raman and IR experiments performed on water at room temperature.^{65,66} The translational, librational, OH bending, and OH stretching frequencies observed around 100, 600, 1600, and 3400 cm^{−1}, respectively, are well reproduced by the CP-aiMD simulations for both [PtCl₄]_{sol}^{2−} and H₂O (Figure S1d). The origin of the theoretical red-shift observed mainly above 1200 cm^{−1} have been extensively discussed previously.⁶⁷ On the basis of the VDOS, we conclude that the whole vibrational information about the solvent will be transferred to the NMR calculations.

The quality of the [PtCl₄]_{sol}^{2−} vibrational signature can be assessed by considering the partial VDOS calculated for the isolated complex (Figure S4c in the SI). Therefore, as a second example, we also show the partial VDOS of the isolated [Pt(CN)₄]_{sol}^{2−} complex in Figure S4d. The principal vibrational wave numbers deduced from the power spectrum of the partial

- (56) Kroening, R. F.; Rush, R. M.; Martin, D. S.; Clardy, J. C. *Inorg. Chem.* **1974**, *13*, 1366–1373.
 (57) Chen, X.; Chu, W.; Wang, L.; Wu, Z. *J. Mol. Struct.* **2009**, *920*, 40–44.
 (58) Schefer, J.; Schwarzenbach, D.; Fischer, P.; Koetzle, T.; Larsen, F. K.; Haussühl, S.; Rüdinger, M.; McIntyre, G.; Birkedal, H.; Bürgi, H. *Acta Crystallogr. B* **1998**, *54*, 121–128.
 (59) Grundy, H. D.; Brown, I. D. *Can. J. Chem.* **1970**, *48*, 1151–1154.
 (60) Mühle, C.; Nuss, J.; Dinnebier, R. E.; Jansen, M. *Z. Anorg. Allg. Chem.* **2004**, *630*, 1462–1468.
 (61) Hocking, R. K.; Deeth, R. J.; Hambley, T. W. *Inorg. Chem.* **2007**, *46*, 8238–8244.
 (62) Dub, P. A.; Filippov, O. A.; Belkova, N. V.; Rodriguez-Zubiri, M.; Poli, R. *J. Phys. Chem. A* **2009**, *113*, 6348–6355.

Table 4. Selected Experimental and Theoretical Vibrational Wave Numbers (cm^{-1}) of the $[\text{PtX}_n]^{2-}$ ($\text{X} = \text{Cl}, \text{Br}$ and $n = 4, 6$) and $[\text{Pt}(\text{CN})_4]^{2-}$ Complexes

assignment ^{62,63}	$[\text{Pt}(\text{CN})_4]^{2-}$		$[\text{PtCl}_4]^{2-}$		$[\text{PtBr}_4]^{2-}$		$[\text{PtCl}_6]^{2-}$	$[\text{PtBr}_6]^{2-}$
	ω_{expt}^a	ω_{th}	ω_{expt}^b	ω_{th}	ω_{expt}^c	ω_{th}	ω_{th}	ω_{th}
$\nu_{\text{Pt-X}}$	507(IR)	480	330(R)	330	226(IR)	250	335	365
	464(R)	450	312(R)	295	208(R)	215	295	250
			313(IR)		194(R)			
$\delta_{\text{X-Pt-X}}$			171(R)	200	110(IR)	130	160	200
			165(IR)	160	106(R)	95	120	125
$\nu_{\text{C}\equiv\text{N}}$	2168(R)	2140						
	2146(R)							
	2137(IR)	2090						
	2129(IR)							
$\delta_{\text{Pt-C}\equiv\text{N}}$	411(IR)	410						
	330(R)	350						

^a From Raman and IR experiments realized on a powder of $\text{K}_2\text{Pt}(\text{CN})_4$.⁶⁰ ^b From Raman and IR experiments realized on aqueous solutions of K_2PtCl_4 .⁶³ and $(\text{NBu}_4)_2\text{PtCl}_4$,⁶³ respectively. ^c From Raman and IR experiments realized on aqueous solutions of K_2PtBr_4 and $(\text{PBu}_4)_2\text{PtBr}_4$,⁶² respectively.

VACFs for the whole series of solvated complexes are collected together with experimental values in Table 4. As shown in Figure S4c, a propagation time of 5 ps is sufficient to acquire the vibrational features above 100 cm^{-1} . The latter are related mainly to the Pt–X bonds' stretching ($\nu_{\text{Pt-X}}$) and the X–Pt–X bending modes ($\delta_{\text{X-Pt-X}}$), which are characteristic of the square-planar complexes.⁶³ This also indicates that the slow motions related to the wagging modes, generally observed below 100 cm^{-1} ,⁶² are not completely recovered by the simulations. The overall calculated and experimental wave numbers obtained for $[\text{PtCl}_4]^{2-}$, $[\text{PtBr}_4]^{2-}$, and $[\text{Pt}(\text{CN})_4]^{2-}$ are in nice agreement. The peaks observed around 2100 cm^{-1} for the cyanide complex (Figure S4d) indicate that the stretching modes of the $\text{C}\equiv\text{N}$ bonds have also been activated during the dynamics, which is consistent with IR and Raman observations.⁶⁰ Despite the fact that the partial VDOSs have been computed using classical time correlation functions within the harmonic approximation, the comparison of the calculated “semi-classical” frequencies along with the experimental observations shed some light on the relevance of the simulations.

A more stringent assessment of the predicted vibrational properties would be realized through the computation of the IR absorption coefficient using the formalism of the response theory,⁶⁸ adapted to classical propagation of the nuclei.^{69,70} Nevertheless, considering the number of systems investigated, as well as the quality of the structural and dynamic properties, we can conclude that the sampling of the trajectories used for the computation of the ^{195}Pt shielding properties will be sufficiently representative of the dynamic of the Pt anionic complexes in water solutions. Finally, we emphasize that the possible inaccuracies of the CP-aiMDs, which are expected to be small, might be due to the following three main factors: (i) Overestimation of the GGA bond lengths. (ii) Propagation time, which prevents the observation of complete $[\text{PtX}_n]^{2-}$ wagging

vibrational modes. We estimate that a propagation time around 10 ps should be able to fully recover these modes. (iii) Substitution of the proper counterions by protons. Unfortunately, treatment of larger counterions implies an unwanted increase of the hydration shell, leading to presently unaffordable computational costs.

5. ^{195}Pt Shielding Convergence

A time-dependent NMR observable like the isotropic shielding σ_{obs} can be calculated using its average taken over a long time interval. This yields to the formal relation:

$$\sigma_{\text{obs}} = \langle \sigma(t) \rangle_{\text{time}} = \lim_{t_{\text{obs}} \rightarrow \infty} \frac{1}{t_{\text{obs}}} \int_0^{t_{\text{obs}}} \sigma(\Gamma(t)) dt \quad (1)$$

where $\Gamma(t)$ refers to the configuration of the system at time t .⁷¹ From the “discrete formalism” involved in the computer simulation of liquids, eq 1 must be reformulated in order to show the dependence of $\langle \sigma(t) \rangle_{\text{time}}$ on the discrete sampling:

$$\langle \sigma(t) \rangle_{\text{time}} \approx \langle \sigma(\tau) \rangle_{\text{run}} = \frac{1}{\tau_{\text{max}}} \sum_{\tau=1}^{\tau_{\text{max}}} \sigma(\Gamma(\tau)) \quad (2)$$

Here, τ indicates an index running over the series of time steps of length $\Delta t = t_{\text{run}}/\tau_{\text{max}}$, with t_{run} and τ_{max} being the total time length of the simulation (here 5 ps) and the total number of configurations used for the sampling, respectively. We emphasize that eq 2 holds for a physical quantity obeying Gaussian-like statistics. For well-equilibrated systems and considering a sampling of the microcanonical ensemble, the distribution of the calculated chemical shifts should respect approximately this condition.^{72,73}

As emphasized previously, experiments measure a NMR response averaged over all the probe nuclei present in the sample and over a time scale which cannot be reached by computer simulations (even with fast classical MD). Thus, we must be able to evaluate the statistical error as well as possible systematic errors which limit the reliability of the predicted chemical shifts. For example, the ^{195}Pt shielding distribution obtained for the

(63) Goggin, P. L.; Mink, J. *J. Chem. Soc., Dalton Trans.* **1974**, 1479–1483.

(64) Santra, B.; Michaelides, A.; Scheffler, M. *J. Chem. Phys.* **2009**, *131*, 124509–9.

(65) Kim, J.; Schmitt, U. W.; Gruetzmacher, J. A.; Voth, G. A.; Scherer, N. E. *J. Chem. Phys.* **2002**, *116*, 737–746.

(66) Carey, D. M.; Korenowski, G. M. *J. Chem. Phys.* **1998**, *108*, 2669–2675.

(67) Lee, H.; Tuckerman, M. E. *J. Chem. Phys.* **2007**, *126*, 164501–16.

(68) McQuarrie, D. A. *Statistical Mechanics*, 2nd ed.; University Science Books: Mill Valley, CA, 2000.

(69) Bader, J. S.; Berne, B. J. *J. Chem. Phys.* **1994**, *100*, 8359–8366.

(70) Ifimie, R.; Tuckerman, M. E. *J. Chem. Phys.* **2005**, *122*, 214508–11.

(71) Allen, M. P.; Tildesley, D. J. *Computer Simulation of Liquids*; Oxford University Press: New York, 1989.

(72) Sebastiani, D.; Parrinello, M. *ChemPhysChem* **2002**, *3*, 675–679.

(73) Murakhina, T.; Heuft, J.; Meijer, E. J.; Sebastiani, D. *ChemPhysChem* **2006**, *7*, 2578–2584.

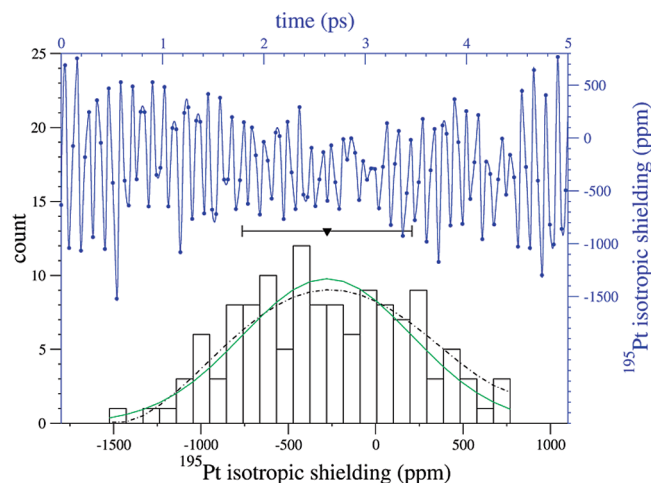


Figure 4. Evolution of the platinum NMR shielding in $[\text{PtCl}_4 \cdot 12(\text{H}_2\text{O})]^{2-}$ during the aiMD (blue) and the corresponding distribution accumulated over 128 configurations (black). The scalar-relativistic ZORA Hamiltonian along with the basis set described in section 2 have been used for these calculations. The green solid line and black dashed line are Gaussian and polynomial (order-3) fits. The average shielding and standard deviation are indicated by the down triangle and the horizontal bar, respectively.

$[\text{PtCl}_4]^{2-}$ complex surrounded by 12 water molecules (noted $[\text{PtCl}_4 \cdot 12(\text{H}_2\text{O})]^{2-}$) is plotted in Figure 4, along with its instantaneous evolution with respect to the aiMD time. In this case, we have considered a sampling of $\tau_{\text{max}} = 128$ configurations ($\Delta t \approx 40$ fs); each configuration is composed of a Pt anionic complex surrounded by the 12 nearest H_2O molecules isolated from the bulk. For this section, all results were obtained from scalar ZORA computations to save computational cost. From Figure 4, we observe that the large range of variation of $\sigma(^{195}\text{Pt})$ values (about 2300 ppm) is responsible for the large spread of the distribution, the corresponding standard deviation (noted s) being equal to 486 ppm. The distribution resembles a bell curve centered at the mean value of -278 ppm. The Gaussian and polynomial fits are also plotted for comparison in Figure 4. The same distribution shapes have been observed for the other solvated complexes studied in this work. The large half-width of the Gaussian function reflects the strong influence of the structural parameters on the shielding constants. Given the standard deviations of the Pt–X bond lengths R_X (see Table 3), we can evaluate the variation of the shielding with respect to R_X , i.e., $\partial\sigma/\partial R_X$, to be roughly between 190 and 230 $\text{ppm} \cdot \text{pm}^{-1}$ and around 50 $\text{ppm} \cdot \text{pm}^{-1}$ for the halide complexes and $[\text{Pt}(\text{CN})_4]^{2-}$, respectively.

Another important aspect of MD simulations is to verify the convergence of the computed physical observable(s) with respect to the sampling method used, such as the number of configurations τ_{max} involved in eq 2 and the corresponding time step Δt . It is well-known that the phase space points $\Gamma(t)$ can be time-correlated if Δt is lower than the characteristic correlation time. The blocking method can be employed to detect such correlation.⁷⁴ We have confirmed that the data points used for the averages in this work are statistically uncorrelated.⁷⁵ The notions of statically uncorrelated sampling or, conversely, statistical inefficiency allow also us to estimate the statistical significance of the results.^{71,76} The calculated average $\langle\sigma(^{195}\text{Pt})\rangle$ in

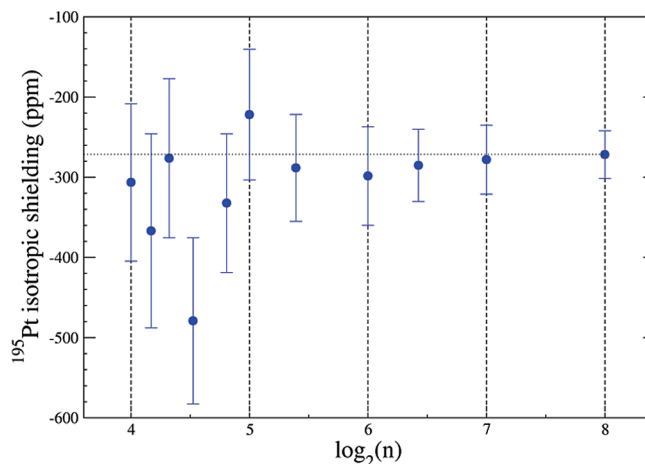


Figure 5. Platinum NMR shielding in $[\text{PtCl}_4 \cdot 12(\text{H}_2\text{O})]^{2-}$ as a function of the number n of statistically uncorrelated points defining the maximum number of configurations $\tau_{\text{max}} = 2^n$ in eq 2. The vertical bars indicate the statistical error \bar{s} . The scalar-relativistic ZORA Hamiltonian and the basis set described in section 2 have been used for these calculations.

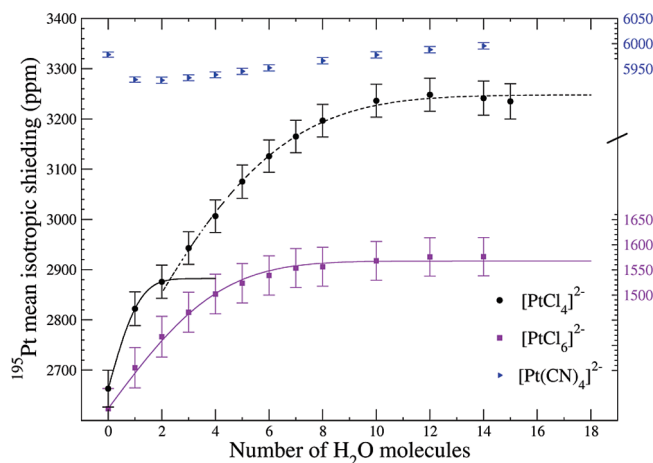


Figure 6. Convergence of the platinum NMR shielding in the $[\text{PtCl}_n \cdot x(\text{H}_2\text{O})]^{2-}$ and $[\text{Pt}(\text{CN})_4 \cdot x(\text{H}_2\text{O})]^{2-}$ solvated complexes as a function of the number of water molecules x . The y-scale of each curve has been adapted in order to span a range of 800 ppm. Nonlinear curve fits using the error function are represented by solid and dashed lines (see text for explanation). Vertical bars represent the statistical error \bar{s} . Each data point involves a sampling of 128 aiMD configurations over 5 ps.

$[\text{PtCl}_4 \cdot 12(\text{H}_2\text{O})]^{2-}$ as a function of τ_{max} is plotted in Figure 5, considering an equally spaced sampling. A smooth convergence of the shielding is observed for $\tau_{\text{max}} \geq 2^5$. Given the simulation time of the aiMD, the best compromise between statistical efficiency and computational cost is obtained for $\tau_{\text{max}} = 2^7$, with a statistical error $\bar{s} = s/\sqrt{\tau_{\text{max}}} = 43$ ppm. Therefore, in the following, the ^{195}Pt chemical shifts for the set of $[\text{PtX}_n \cdot x(\text{H}_2\text{O})]^{2-}$ solvated systems have been obtained using 128 configurations.

6. ^{195}Pt Shielding Induced by the Solvent

Convergence of the ^{195}Pt isotropic shielding as a function of the number of water molecules constituting the first hydration shell around the complex is plotted in Figure 6 for $[\text{PtCl}_4]^{2-}$, $[\text{PtCl}_6]^{2-}$, and $[\text{Pt}(\text{CN})_4]^{2-}$. Results obtained for $[\text{PtBr}_4]^{2-}$ and $[\text{PtBr}_6]^{2-}$ are presented in the Figure 7. The charged $[\text{PtX}_n \cdot x(\text{H}_2\text{O})]^{2-}$ clusters were built by using an algorithm which considers a number x of shortest $\text{Pt} \cdots \text{O}$ distances and recon-

(74) Flyvbjerg, H.; Petersen, H. G. *J. Chem. Phys.* **1989**, *91*, 461–466.

(75) Kundrat, M. D.; Autschbach, J. *J. Chem. Theor. Comput.* **2008**, *4*, 1902–1914.

(76) Friedberg, R.; Cameron, J. E. *J. Chem. Phys.* **1970**, *52*, 6049–6058.

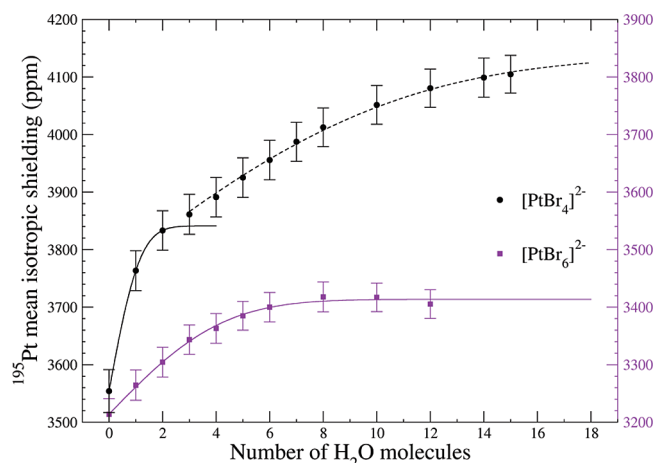


Figure 7. Convergence of the platinum NMR shielding in the $[\text{PtBr}_n \cdot x(\text{H}_2\text{O})]^{2-}$ solvated complexes as a function of the number of water molecules x . The y-scale of each curve have been adapted in order to span a range of 700 ppm. See also the caption of Figure 6.

structures the coordination sphere of each solvent molecule, taking care to avoid the presence of H_3O^+ entities, for each configuration involved in the calculation of $\langle\sigma(^{195}\text{Pt})\rangle$ using eq 2. These and all other calculations in this section have been carried out at the spin-orbit ZORA level of theory. First, from Figures 6 and 7 we observe that the convergence of $\langle\sigma(^{195}\text{Pt})\rangle$ as a function of x is monotonic for all complexes. Interestingly, the influence of the hydration shell on the ^{195}Pt shielding in the cyanide complex is negligible compared to that in the halides analogues, with total solvent effects of 10 ppm for $[\text{Pt}(\text{CN})_4]^{2-}$ vs 190–620 ppm for $[\text{PtCl}_n]^{2-}$ and $[\text{PtBr}_n]^{2-}$, depending on the ligand and the coordination number n . Second, the $\langle\sigma(^{195}\text{Pt})\rangle$ convergence related to the octahedral systems is faster compared to that of the D_{4h} square-planar ones. In the former case, the plateau is reached for a lower number of H_2O molecules, around 8 for $[\text{PtCl}_6]^{2-}$ and $[\text{PtBr}_6]^{2-}$, compared to 12 and 14 for $[\text{PtCl}_4]^{2-}$ and $[\text{PtBr}_4]^{2-}$, respectively. These results corroborate nicely the previous findings based on the analysis of the RDFs, suggesting the existence of an intermediate solvation shell for the halide complexes, whereas this characteristic is absent for the cyanide analogue (see section 3). Furthermore, from integration of the Pt–O RDFs (see Table 1), we find that the numbers of solvent molecules forming the “water-bulk-decorrelated” $[\text{PtX}_n \cdot x(\text{H}_2\text{O})]^{2-}$ clusters are around 10 for the octahedral systems compared to 12 and 14 for $[\text{PtCl}_4]^{2-}$ and $[\text{PtBr}_4]^{2-}$, respectively, which is consistent with the $\langle\sigma(^{195}\text{Pt})\rangle$ convergence analysis presented in Figures 6 and 7. Third, the different convergence behaviors observed between the $[\text{PtX}_6]^{2-}$ and $[\text{PtX}_4]^{2-}$ molecular systems are clearly related to their structural properties, i.e., octahedral vs square-planar.

It is then tempting to go beyond these primary observations by fitting the convergence laws of Figures 6 and 7 in order to find possible connections between the solvent-induced ^{195}Pt shielding and, for example, the geometrical properties of the Pt complexes. The data points show an approximately linear increase of the solvent effects on $\langle\sigma(^{195}\text{Pt})\rangle$ for small number of water molecules and a plateau for larger solvent shells which is reached between 10 and 14 solvent molecules, suggesting that a low-order polynomial fit would not be the most appropriate. Therefore, nonlinear curve fits have been carried out using the following function,

$$\langle\sigma(^{195}\text{Pt})\rangle = \langle\sigma(x)\rangle = \langle\sigma_{\text{bare}}\rangle + \kappa \operatorname{erf}(\alpha x) \quad (3)$$

where $\langle\sigma_{\text{bare}}\rangle$ is the average shielding obtained from the isolated complex, i.e., without the presence of an explicit water shell in the NMR calculations, κ and α are fitting coefficients, and erf is the Gauss error function.⁷⁷ The principal parameters obtained from the various fits are collected in Table 5. Considering the correlation coefficient of 0.998 for both $[\text{PtCl}_6]^{2-}$ and $[\text{PtBr}_6]^{2-}$, we observe that the error function of eq 3 matches very well the convergence laws depicted in Figures 6 and 7. In order to better understand the results obtained for square-planar complexes, we must consider the results obtained from the analysis of the Pt–O and Pt–H RDFs (see section 3), revealing the presence of two weakly bonded water molecules in the axial region of the square-planar complexes (see Table 2). On the basis of these observations, we can decompose the convergence laws in two regions, depending on the value of x : (i) For $0 \leq x \leq 2$, $\langle\sigma(^{195}\text{Pt})\rangle$ increases rapidly due to the fact that weakly bound solvent molecules are close to the metal center (depicted by solid lines in Figures 6 and 7 for $[\text{PtCl}_4]^{2-}$ and $[\text{PtBr}_4]^{2-}$, respectively). (ii) For $x > 2$, $\langle\sigma(^{195}\text{Pt})\rangle$ increases more slowly, and we observe that the fits deriving from eq 3 lead to a reliability comparable to that obtained for the octahedral complexes, with $R = 0.998$ and 0.999 for $[\text{PtCl}_4]^{2-}$ and $[\text{PtBr}_4]^{2-}$, respectively (depicted by dashed lines in Figures 6 and 7). It should be noted that the influence of the axial water molecules is more dominant for $[\text{PtBr}_4]^{2-}$ compared to $[\text{PtCl}_4]^{2-}$. In the former case, σ_{bare} used for the fit is equal to the average shielding obtained for $[\text{PtBr}_4 \cdot 2(\text{H}_2\text{O})]^{2-}$.

At this point, it is interesting to connect the fitted κ and α parameters of eq 3 with characteristic structural quantities of the complexes. Here, we present an attempt to quantify the influence of solvent on the shielding of a metal center in an inorganic complex. In Figure 8, we have plotted the variation of the κ coefficient as a function of the ratio of the charge ($q = 2e$) to the solvent-accessible surface area (ASA). The ASAs were calculated using the method introduced by Richards et al. and optimized by Connolly.^{78–80} The ASA values are listed in Table 5. As shown in Figure 8, the κ coefficient is closely correlated to the q/ASA values by a nonlinear relation, leading us to conclude that the larger is q/ASA , the higher is the strength of the solvent-induced ^{195}Pt shielding. This result is intuitively consistent with the fact that the higher the charge surface density is, the stronger should be the interaction with surrounding polar solvent molecules. Such types of correlations involving the q/ASA or q/V ratio, where V is the volume of the system, have been previously reported for rationalize the variation of the solvation energies and the electron affinity calculated for polyoxometalate clusters.^{81,82}

No obvious correlations linking the α coefficient of eq 3, which governs the convergence rate of $\langle\sigma(^{195}\text{Pt})\rangle$ with respect to the number of water molecules, with structural or physical properties have been found. This is mainly due to the fact that the convergence discontinuity, mainly observed for $[\text{PtBr}_4]^{2-}$,

(77) Abramowitz, M.; Stegun, I. A. *Handbook of Mathematical Functions: with Formulas, Graphs, and Mathematical Tables*; Dover Publications: New York, 1965.

(78) Connolly, M. *Science* **1983**, 221, 709–713.

(79) Lee, B.; Richards, F. J. *Mol. Biol.* **1971**, 55, 379–400.

(80) Connolly, M. L. *J. Appl. Crystallogr.* **1983**, 16, 548–558.

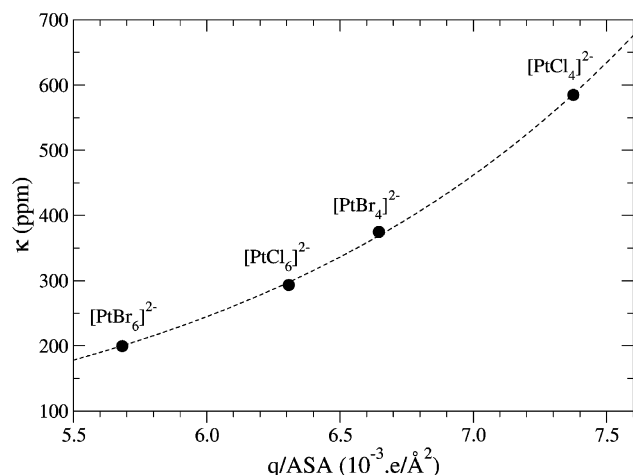
(81) Lopez, X.; Fernandez, J. A.; Poblet, J. M. *Dalton Trans.* **2006**, 1162–1167.

(82) Bagno, A.; Bonchio, M.; Autschbach, J. *Chem.—Eur. J.* **2006**, 12, 8460–8471.

Table 5. Parameters Obtained from the Nonlinear Fits of $\langle\sigma(^{195}\text{Pt})\rangle$ as a Function of x in the $[\text{PtX}_n \cdot x(\text{H}_2\text{O})]^{2-}$ Clusters, Using Eq 3; Correlation Coefficient R Is Also Given, along with the Calculated Accessible Surface Area (ASA) of the Halide Complexes

complex	$\langle\sigma_{\text{bare}}\rangle$ (ppm)	κ (ppm)	α	R	ASA ^a (Å ²)
$[\text{PtCl}_4]^{2-}$ ^b	2663	584.7	0.149	0.9982	272
$[\text{PtBr}_4]^{2-}$ ^c	3763	374.7	0.083	0.9991	301
$[\text{PtCl}_6]^{2-}$	1274	293.4	0.216	0.9977	317
$[\text{PtBr}_6]^{2-}$	3214	199.6	0.213	0.9979	352

^a Calculated using a probe radius of 1.4 Å.⁷⁸ ^b The corresponding curve is shown as a dashed line in Figure 6. ^c In that case, $\langle\sigma_{\text{bare}}\rangle$ is the averaged shielding obtained from the isolated $[\text{PtBr}_4 \cdot 2(\text{H}_2\text{O})]^{2-}$. The corresponding curve is shown as a dashed line in Figure 7.

**Figure 8.** Variation of the solvent-induced ^{195}Pt shielding measured by the κ coefficient of eq 3 as a function of the charge/surface ratio. The dashed line serves as a guide to the eye.

prohibits a possible global rationalization using our simple model. Further investigations are needed in order to find a more stringent model, which could be used for an accurate prediction of the solvent effect on the metal shieldings of solvated complexes.

7. ^{195}Pt Shielding and Chemical Shift Analysis

Liquid-state NMR experiments allow us to determine the strength of the nuclear magnetic shielding of a nucleus through the measurement of the isotropic chemical shift δ . In computational studies where the shielding constants for the probe and a reference (ref) nucleus are computed directly, the averaged chemical shift is

$$\langle\delta\rangle = \frac{\langle\sigma^{\text{ref}}\rangle - \langle\sigma\rangle}{1 - \langle\sigma^{\text{ref}}\rangle} \quad (4)$$

in terms of time-averaged isotropic shielding components $\langle\sigma\rangle$. The denominator $1 - \langle\sigma^{\text{ref}}\rangle$ arises from the definition of the chemical shift where the reference frequency is in the denominator. Usually, the approximation $1 - \langle\sigma^{\text{ref}}\rangle \approx 1$ is made in computational studies, which makes it particularly easy to convert between different references. For heavy nuclei such as ^{195}Pt , neglecting the reference shielding in the denominator may lead to differences in the reported chemical shifts on the order of a percent. In the following, calculations of the time-averaged ^{195}Pt chemical shifts $\langle\delta(^{195}\text{Pt})\rangle$ were obtained with values of $\langle\sigma(^{195}\text{Pt})\rangle$ converged with respect to the water shell size (see section 6) and $[\text{PtCl}_6]^{2-}$ as the reference system.

The use of aiMD for the calculation of a time-averaged property allows us to decompose the calculated ^{195}Pt NMR shielding as

$$\langle\sigma^T\rangle = \sigma_{\text{av}}^T + \langle\Delta\sigma_{\text{vib}}^T\rangle + \langle\Delta\sigma_{\text{solv}}^T\rangle \quad (5)$$

where σ_{av}^T is equal to the shielding obtained from the aiMD “averaged geometry”, the latter being deduced from a single-point calculation performed with the thermally averaged structure at $T \approx 300$ K. The term $\langle\Delta\sigma_{\text{vib}}^T\rangle$ was obtained from an MD average of the shielding without any solvent present, decomposed as $\sigma_{\text{av}}^T + \langle\Delta\sigma_{\text{vib}}^T\rangle$. The solvent term then represents the difference between the MD averages with and without explicit solvent. The parameters used to generate the averaged structures are listed in Table 3.

We emphasize here that σ_{av}^T should not be identified with an effective vibrationally averaged shielding σ_{eff} that is obtained upon quantum-vibrationally averaging molecular properties.^{83–85} The zero-point energy corrections are not present in aiMD that treats the nuclei classically. For the heavy nuclei in our samples at experimentally relevant temperatures, however, this classical motion on the quantum-mechanical potential energy surface should provide a reasonable description of the average complex structure and the effect of vibrational motion on their NMR parameters. The aiMD being based on the classical propagation of the nuclei, no quantum vibrations can be observed at 0 K. As a result, connections between the shielding contributions presented in eq 5 and the ones obtained from a perturbation expansion of the shielding around a zero-point effective geometry are not straightforward and are beyond the scope of this paper. We notice here that the zero-point vibrational corrections have been found to be lower than -100 ppm for 3d transition metal shieldings.^{84,86} As emphasized by Bühl et al., if we consider the relative chemical shift these contributions almost cancel.⁸⁴

The second and third terms of eq 5, namely $\langle\Delta\sigma_{\text{vib}}^T\rangle$ and $\langle\Delta\sigma_{\text{solv}}^T\rangle$, are the time-averaged corrections due to the thermally activated rovibrational and solvent effects. For consistency with eq 3, we point out that $\langle\sigma_{\text{bare}}\rangle = \sigma_{\text{av}}^T + \langle\Delta\sigma_{\text{vib}}^T\rangle$ and that the fitting coefficient κ should be close to the value of $\langle\Delta\sigma_{\text{solv}}^T\rangle$. The superscript T in $\langle\Delta\sigma_{\text{solv}}^T\rangle$ means that the solvent effects on $\langle\sigma(^{195}\text{Pt})\rangle$ are thermally averaged as for $\langle\Delta\sigma_{\text{vib}}^T\rangle$. The analogue of eq 5 can be introduced to define the different contributions of the chemical shift, by

$$\langle\delta^T\rangle = \delta_{\text{av}}^T + \Delta\langle\delta_{\text{vib}}^T\rangle + \Delta\langle\delta_{\text{solv}}^T\rangle \quad (6)$$

where δ_{av}^T , $\Delta\langle\delta_{\text{vib}}^T\rangle$, and $\Delta\langle\delta_{\text{solv}}^T\rangle$ are calculated from the components of eqs 5 obtained for the probed and reference Pt complexes, using eq 4.

Contributions arising from eqs 5 and 6 are presented in Table 6 for the whole set of Pt anionic complexes studied in this work. Time-averaged isotropic shieldings and chemical shifts used for

Table 6. Decomposition of the ^{195}Pt Calculated Isotropic Shielding and Chemical Shift (in ppm) Following Eqs 5 and 6, Respectively, and the Influence of the Relativistic Effects

complex	Ham. ^a	shielding				chemical shift				expt
		σ_{av}^T	$\langle\Delta\sigma_{\text{vib}}^T\rangle$	$\langle\Delta\sigma_{\text{solv}}^T\rangle$	sum \pm \bar{s}^b	δ_{av}^T	$\Delta\langle\delta_{\text{vib}}^T\rangle$	$\Delta\langle\delta_{\text{solv}}^T\rangle$	sum \pm \bar{s}^b	
[PtCl ₆] ²⁻ ^c	SO	1340	−66	303	1576 \pm 38	—	—	—	—	—
	SC				−2063 \pm 44					
	NR				426 \pm 28					
[PtCl ₄] ²⁻	SO	2702	−39	572	3235 \pm 35	−1364	−27	−270	−1661 \pm 73	−1623 ^d
	SC				−278 \pm 43				−1782 \pm 87	
	NR				1536 \pm 28				−1110 \pm 56	
[PtBr ₄] ²⁻	SO	3665	−111	551	4105 \pm 33	−2329	45	−248	−2532 \pm 71	−2672 ^d
	SC				209 \pm 39				−2268 \pm 83	
	NR				2316 \pm 24				−1890 \pm 52	
[PtBr ₆] ²⁻	SO	3299	−85	191	3405 \pm 25	−1962	19	111	−1832 \pm 63	−1882 ^e
	SC				−933 \pm 30				−1128 \pm 74	
	NR				1714 \pm 19				−1288 \pm 47	
[Pt(CN) ₄] ²⁻	SO	6068	−90	17	5996 \pm 6	−4728	18	284	−4426 \pm 44	−4746 ^f
	SC				2932 \pm 8				−4485 \pm 52	
	NR				3536 \pm 7				−3111 \pm 35	

^a Hamiltonian; NR, SC, and SO stand for the nonrelativistic, scalar ZORA, and spin-orbit ZORA Hamiltonian, respectively. ^b Sum of the contributions along with the statistical error \bar{s} . ^c Reference used for the calculation of the ^{195}Pt chemical shifts. ^d Reference 87. ^e Reference 88. ^f Reference 89.

this purpose are collected in Table S1 of the SI. Influences of $\langle\Delta\sigma_{\text{vib}}^T\rangle$ on the isotropic shielding range from −40 to −110 ppm, depending on both the type and number of ligands. The magnitude and the sign of the vibrational contributions observed for $\langle\sigma(^{195}\text{Pt})\rangle$ are consistent with previous findings obtained for 3d transition metal complexes.⁸⁶ For the halide complexes, this vibrational deshielding effect is overpowered by the large solvent-induced shielding contribution $\langle\Delta\sigma_{\text{solv}}^T\rangle$, which reaches a value of 572 ppm for [PtCl₄]²⁻. As noticed in section 6, the first hydration shell surrounding the complex has a strong impact on $\langle\sigma(^{195}\text{Pt})\rangle$ in anionic halide complexes, whereas for the square-planar cyano complex the solvent effects are negligible. We emphasize that the solvent-induced shielding represents from 6% ([PtBr₆]²⁻) to 19% ([PtCl₄]²⁻) of the overall isotropic shielding. Comparing the $\langle\Delta\sigma_{\text{solv}}^T\rangle$ of 572 and 551 ppm reached for [PtCl₄]²⁻ and [PtBr₄]²⁻ with the values of 303 and 191 ppm obtained for [PtCl₆]²⁻ and [PtBr₆]²⁻, respectively, we suggest that the larger solvent effects observed for the square-planar complexes reflect the close proximity of the H₂O molecules in their equatorial region (see section 3 and Figure 3). The influence of this particular structural property on the ^{195}Pt NMR shielding and chemical shift in anionic square-planar complexes will be addressed in a future paper.

From the point of view of the ^{195}Pt chemical shift, the difference in magnitude of $\langle\Delta\sigma_{\text{vib}}^T\rangle$ led to residual vibrational contributions of $\langle\delta^T\rangle$ between −27 and 45 ppm. Considering the magnitudes ranging from −270 to 111 ppm which have been obtained for $\Delta\langle\delta_{\text{solv}}^T\rangle$, we can conclude that the solvent-induced chemical shifts are more important than vibrational corrections. It should be emphasized that the sizable value of 284 ppm calculated for [Pt(CN)₄]²⁻ is entirely governed by the $\Delta\langle\sigma_{\text{solv}}^T\rangle$ of the reference system, [PtCl₆]²⁻. As shown in Table 6, the

solvent-induced ^{195}Pt chemical shifts are different, both in magnitude and in sign, demonstrating the necessity of explicitly including the solvent in the computational models.

We now compare the theoretical and experimental ^{195}Pt chemical shifts. Bearing in mind the statistical errors in the calculations, a good agreement with experiment is obtained at the spin-orbit ZORA level of approximation for [PtCl₄]²⁻, [PtBr₆]²⁻, and to a lesser extent [PtBr₄]²⁻; the deviations from experiment range between 2 and 5% (Table 6). For the cyano complex, the slightly larger deviation of 7% may be related to the inaccuracies inherent to use of the “pure” GGA functional.¹⁴ A spin-orbit ZORA hybrid functional method for NMR shielding tensors has just recently been developed by Krykunov et al.⁹⁰ For ^{195}Pt chemical shifts in a related set of Pt(IV) complexes, only a modest improvement of the B3LYP hybrid over pure functionals was obtained, with root-mean-square deviations from experiment dropping from 298 (B3LYP) to 265 ppm (BLYP). Unfortunately, dynamical and solvent effects and different Pt oxidation states were not taken into account in the assessment of the hybrid functional performance. Once the required exchange–correlation response kernels have been implemented, it will be interesting to test the performance of other, more flexible hybrids such as the MO6 family,⁹¹ but for a fair assessment it would then also be important to use such a functional in the aiMD simulations.

A potential source of error in the computations is the replacement of the counterions by H⁺. Fortunately, it has been demonstrated that ion pair formation and its effects on ^{195}Pt shifts are essentially insignificant for aqueous solutions, even for high concentrations.⁹²

For completeness, ^{195}Pt chemical shift calculations have also been performed using a nonrelativistic and the scalar ZORA Hamiltonians (see Table 6). As expected, the nonrelativistic results do not reproduce the experimental values, with discrepancies of up to 34%. Inclusion of scalar relativistic effects improves the correlation between the calculations and experiment, with absolute deviations of 10, 15, and 5% for [PtCl₄]²⁻,

(83) Ruud, K.; Astrand, P.; Taylor, P. R. *J. Chem. Phys.* **2000**, *112*, 2668–2683.

(84) Grigoleit, S.; Bühl, M. *Chem.—Eur. J.* **2004**, *10*, 5541–5552.

(85) Mort, B. C.; Autschbach, J. J. *Am. Chem. Soc.* **2006**, *128*, 10060–10072.

(86) Bühl, M.; Imhof, P.; Repisky, M. *ChemPhysChem* **2004**, *5*, 410–414.

(87) Matsumoto, K.; Arai, S.; Ochiai, M.; Chen, W.; Nakata, A.; Nakai, H.; Kinoshita, S. *Inorg. Chem.* **2005**, *44*, 8552–8560.

(88) Kramer, J.; Koch, K. R. *Inorg. Chem.* **2007**, *46*, 7466–7476.

(89) Maliarik, M.; Berg, K.; Glaser, J.; Sandstrom, M.; Toth, I. *Inorg. Chem.* **1998**, *37*, 2910–2919.

(90) Krykunov, M.; Ziegler, T.; van Lenthe, E. *J. Phys. Chem. A* **2009**, *113*, 11495–11500.

(91) Zhao, Y.; Truhlar, D. G. *Acc. Chem. Res.* **2008**, *41*, 157–167.

(92) Naidoo, K. J.; Lopis, A. S.; Westra, A. N.; Robinson, D. J.; Koch, K. R. *J. Am. Chem. Soc.* **2003**, *125*, 13330–13331.

[PtBr₄]²⁻, and [Pt(CN)₄]²⁻, respectively. An exception is [PtBr₆]²⁻, where the deviation from experiment reaches a value of 700 ppm (deviation of 40%). Extension of the level of theory to the spin–orbit interaction corrects this large deviation. The data demonstrate how, for the series CN < Cl < Br, the influence of spin–orbit coupling from a heavy-atom neighbor on a heavy nucleus shielding (a HAOHA effect¹⁰) increases. As previously discussed,⁹³ this trend is related to the influence of the spin–orbit interaction at the ligand atom upon the chemical shift of the metal center, which in the case of Br in platinum–bromine complexes is the dominant component compared to the spin–orbit effect of the metal center.

8. Conclusions and Outlook

As previously pointed out in many reviews,^{8–10,94} structural-, vibrational-, solvent-, and relativity-induced shielding effects are of primary importance for the computation of NMR shielding constants and shielding tensors of heavy atoms and, by extension, for the prediction of chemical shifts in inorganic and organometallic systems in solution. Methodologies derived for the computation of NMR properties on isolated molecules, which in the better case include zero-point vibrational corrections and solvent-induced polarization being represented at least at the level of a continuum model, can be insufficient to recover the fundamental effects due to the thermally activated motions of the probed system—coupled to the motion of the solvent—along with the strong influence of the environment. In this work we have demonstrated that a combination of *ab initio* molecular dynamics and relativistic NMR methods based on DFT allow us to overcome these intricacies, leading for our test set to an agreement within 10% for the calculated ¹⁹⁵Pt chemical shifts with respect to the liquid-state NMR experiments.

Beyond this good agreement, the main conclusion emerging from this work is that ¹⁹⁵Pt liquid-state NMR parameters may give access to information about the solvation shell organization, for instance. We have demonstrated that the different behavior of ¹⁹⁵Pt NMR parameters with respect to the solvent effects can

be directly connected to the solution structure of the complex. We emphasize that the strength of the solvent effects is closely related to the ligand nature, i.e., σ -donor/ π -back-acceptor for CN vs mainly σ coordinating coupled to a strong electronic inductive effect for the halides, and the geometry, i.e., octahedral vs square-planar. Further investigations should be conducted in order to fully understand the electronic process responsible for the magnitude of solvent-induced shielding mediated by the ligand on the ¹⁹⁵Pt NMR response. We have found a correlation with the surface-charge density superimposed onto more specific inner-shell effects in the case of the square-planar systems. Conversely, from the liquid-state NMR point of view, it appears that the observed ¹⁹⁵Pt chemical shifts can also include a solvent shell fingerprint.

In the future, a combination of aiMD dynamics with first-principles NMR calculations and liquid-state NMR measurements, perhaps in conjunction with solid-state NMR measurements and computations for the solid state, might also be useful to assess the reliability of various exchange-correlation functionals for the purpose of computing nuclear NMR parameters for heavy nuclei such as W, Pt, Hg, Tl, and Pb, where “cross terms” between relativistic effects and geometry, environment, or electron correlation (to name a few influences) can be significant.

Acknowledgment. The authors are grateful for financial support from the National Science Foundation (CHE CHE-0447321) and acknowledge support from the Center for Computational Research at the University at Buffalo for the research reported here. L.A.T. gratefully acknowledges D. Hache for preparing some of the graphics.

Supporting Information Available: Details about the calculation of the RDFs and VACFs; analysis of the RDFs in pure water and for the [PtCl₄]_{sol}²⁻ system; additional RDFs for the halide complexes; aiMD averaged shielding constants for each complex calculated at different levels of theory; complete refs 27 and 35. This material is available free of charge via the Internet at <http://pubs.acs.org>.

JA9096863

(93) Autschbach, J.; Zheng, S. *Magn. Reson. Chem.* **2008**, *46*, S45–S55.

(94) Vaara, J. *Phys. Chem. Chem. Phys.* **2007**, *9*, 5399–5418.